The Release of Inertial Instability near an Idealized Zonal Jet

Callum F. Thompson[1] and David M. Schultz[2,3]

[1]Earth Research Institute, Department of Geography, University of California, Santa Barbara, Ellison Hall, Isla Vista, CA 93117, United States

[2]Centre for Atmospheric Science, Department of Earth and Environmental Sciences, The University of Manchester, Oxford Rd, Manchester M13 9PL, United Kingdom

[3]Centre for Crisis Studies and Mitigation, The University of Manchester, Oxford Rd, Manchester M13 9PL, United Kingdom

Key Points:

- Inertial instability is released through ribbon-like layers of enhanced meridional wind and the radiation of inertia–gravity waves.
- Layers of meridional wind are up to 7 m s^{-1} in magnitude, extend 100 km across the jet, and persist for 11 days.
- Inertial instability release also produces moderate occurrences of clear-air turbulence, as diagnosed by the Ellrod–Knapp Turbulence Index.

Corresponding author: Callum F. Thompson, thompson.callum@yahoo.co.uk

Abstract

Inertial instability is a hydrodynamic instability that occurs in strong anticyclonic flow and is typically diagnosed by negative absolute vorticity in the Northern Hemisphere. As such, inertial instability is often observed on the anticyclonic-shear side of jet streams, yet the release of the instability in this environment is still poorly understood. We construct an idealized midlatitude zonal jet and perform two experiments: one control simulation with no inertial instability and one experiment with inertial instability simulating its release. We find that the release of the instability results in meridional wind perturbations of up to 7 m s^{-1} over 200 km that persist for several days, in addition to radiating inertia–gravity waves several hundreds of kilometers away from the unstable region. Furthermore, these perturbations instigate light–moderate occurrences of clear-air turbulence around the unstable region that persist for up to 12 hours.

Plain Language Summary

The jet stream is a narrow region of strong westerly winds above the Earth's surface over the midlatitudes in the Northern and Southern Hemispheres. When winds speeds decrease too sharply laterally on the equatorward side of the jet stream, the flow is said to be in state of inertial instability. However, how the atmosphere responds to the instability in this situation is not well understood. To gain a better understanding, we used a numerical model to simulate an idealized jet stream with inertial instability against a control jet stream with no instability. We find that the simulation with the instability produced stationary ribbon-shaped circulations along the jet within the unstable region, in addition to circulations called inertia–gravity waves that propagate several hundred kilometers away from the unstable region. Although these inertia–gravity waves have been hypothesized to instigate clear-air turbulence, we find that the ribbon-shaped regions of enhanced north–south winds themselves instigate light–moderate instances of clear-air turbulence that can last for up to 12 hours. Further research on whether this result is found in the real atmosphere has the potential to improve weather forecasts for the aviation sector.

1 Introduction

Inertial instability describes an imbalance on air pacels between the horizontal pressure-gradient and Coriolis forces in a zonal flow, typically diagnosed when the anticyclonic

absolute vorticity exceeds the Coriolis parameter (e.g., negative absolute vorticity in the Northern Hemisphere) (Knox, 2003). Inertial instability therefore occurs in environments of strong anticyclonic shear or curvature, such as the equatorward side of jet streams (Knox, 1997; Schumacher & Schultz, 2001; Thompson et al., 2018).

Although the existence of inertial instability in such environments had previously been doubted (Blumen & Washington, 1969; Leary, 1974; Holton, 2012), radiosonde observations (Blanchard et al., 1998; Sato & Dunkerton, 2002), the advent of reanalysis (Sato & Dunkerton, 2002; Coniglio et al., 2010; Thompson et al., 2018), and numerical weather prediction models (Schultz & Knox, 2007; Schumacher et al., 2010; Siedersleben & Gohm, 2016) have furnished ample evidence for its occurrence. For example, in examining radiosondes and National Center for Atmospheric Research (NCAR) reanalyses, Sato and Dunkerton (2002) showed that inertial instability was present for more than 30% of winter in the subtropical jet south of Japan. More recently, Thompson et al. (2018) created a 30-yr climatology of tropospheric inertial instability and found that the jet-exit region at 250 hPa in the North Atlantic was inertially unstable for 9% of the period 1979–2014. Such climatological studies put the existence of tropospheric inertial instability on firmer ground.

The question then turns to how is inertial instability released, and what are its impacts in the troposphere, topics that remain poorly understood. The occurrence and release of tropospheric inertial instability has so far been cited to promote upper-level outflow in convective storms (Blanchard et al., 1998; Coniglio et al., 2010) and the organization of linear precipitating bands near mountain ranges (Schultz & Knox, 2007; Schumacher et al., 2010, 2015; Siedersleben & Gohm, 2016). Inertia–gravity wave emission resulting from the release of the instability has also been hypothesized to create clear-air turbulence (CAT) when the waves break (Knox, 1997; Sharman et al., 2012), a recurring cause of in-flight injuries and aircraft damage (Fultz & Ashley, 2016). Understanding the impacts associated with the release of inertial instability is therefore not merely an academic issue, but one that impacts society.

As attributing the effects of inertial instability release can be difficult due to the simultaneous occurrence of other processes in the real atmosphere (Schultz & Knox, 2007), idealized modeling emerges as an effective and more clinical approach. Hence, this letter aims to characterize the release of tropospheric inertial instability by simulating an

idealized zonal midlatitude jet stream using a nonhydrostatic numerical cloud model. We compare two simulations: one initialized with no instability and one initialized with instability on the equatorward side of the jet due to strong anticyclonic shear. From these simulations, we illustrate the structure and longevity of circulations that develop in response to tropospheric inertial instability. In addition, we also test one hypothesis of inertial instability in the case of clear-air turbulence. Accordingly, the rest of this letter is structured as follows: the modeling configuration of our simulations is described in section 2, sections 3 presents our simulation results and their context in the scientific literature, and finally, conclusions are summarized in section 4.

2 Model Set-Up

The model used in this study is Cloud Model 1 (CM1) version 19.4, a nonhydrostatic numerical model (Bryan & Fritsch, 2002), configured to simulate a midlatitude zonal jet in which the degree of inertial stability can be varied. A reference jet with a wind maximum of 30 m s^{-1} and no instability is compared with a 50 m s^{-1} jet with instability on its equatorward side due to stronger anticyclonic-shear vorticity (Figure 1). Each jet is centered at a latitude of 45°N and simulated within a 3000 km × 2000 km channel domain with a horizontal grid spacing of 5 km. In the vertical, 70 levels span 0–21 km with a spacing of 200 m. A free-slip boundary condition is applied at the upper boundary, with a Rayleigh damping layer above 20 km to minimize inertia–gravity-wave reflection. Periodic boundary conditions are imposed at the western and eastern boundaries and open-radiative conditions at the northern and southern boundaries, a set-up typical of many channel simulations (e.g. Plougonven & Snyder, 2005; Terpstra & Spengler, 2015). Planetary boundary layer processes are parameterized according to CM1's GFS-EDMF boundary-layer parameterization scheme (Han et al., 2016). No radiation or convection parameterizations are used and all simulations are of a dry atmosphere in order to suppress the creation of inertial instability via diabatic heating and latent-heat release (e.g. Raymond & Jiang, 1990). Hence, the only source of inertial instability in this study is from the initial condition, described next.

For the initial thermodynamic environment, the base-state is constructed in two layers, characterized by their Brunt–Väisälä frequency (N). The first layer spans 0–11 km where $N = 0.01$ s^{-1}, and the second layer spans 11–21 km where $N = 0.02$ s^{-1}. The thermodynamic base state therefore approximates a troposphere and a stratosphere. For

the zonal jet, the zonal wind in CM1 is the sum of a base-state wind and a perturbation wind. Here, the base-state zonal wind is zero and the perturbation added is that given by Terpstra and Spengler (2015), which is balanced with the meridional gradient of the non-dimensional pressure perturbation in CM1's governing equations to ensure a geostrophically balanced zonal wind, $u_g(y, z)$:

$$u_g(y,z) = \begin{cases} u_0 \sin^3\left[\pi \sin^2\left(\frac{\pi}{2}\frac{y}{L_y}\right)\right] \sin^t\left[\frac{\pi}{2}\left(\frac{z-z_l}{z_0-z_l}\right)\right], & \text{if } |y| \le L_y \text{ and } z_l \le z \le z_0 \\ u_0 \sin^3\left[\pi \sin^2\left(\frac{\pi}{2}\frac{y}{L_y}\right)\right] \sin^s\left[\frac{\pi}{2}\left(\frac{z-z_u}{z_0-z_u}\right)\right], & \text{if } |y| \le L_y \text{ and } z_0 \le z \le z_u \\ 0, \text{ elsewhere.} \end{cases} \quad (1)$$

Here, u_0 is the maximum wind speed centered at z_0, y is the meridional coordinate, z is height, L_y is the width of the jet, z_u and z_l are the upper and lower extents of the jet, and s and t control the shape of the jet above and below z_0 respectively. In this study, $L_y = 2000$ km, $z_0 = 11$ km, $z_u = 21$ km, $z_l = -500$ m, $s = 10$, and $t = 1.5$, giving a realistic jet stream cross-section whose inertial stability can be varied by varying the wind speed maximum, u_0, and hence the degree of anticyclonic-shear vorticity on the equatorward side of the jet. Here, we select two values of u_0: 30 m s^{-1} to create an inertially stable region on the equatorward side of the jet and 50 m s^{-1} to create an inertially unstable region (Figure 1). For a more general jet-stream wind-speed distribution, there is no specific value of maximum wind speed that would determine the presence or absence of inertial instability; the specific value would be a function of the specific mathematical formulation of the jet stream.

Furthermore, with this 50 m s^{-1} wind speed and the associated absolute vorticity, the e-folding time, τ, can be calculated. The e-folding time is the time taken for a meridional wind perturbation within the inertially unstable region to accelerate by a factor of e (≈ 2.71), given by:

$$\tau = \frac{1}{\sqrt{|f(\zeta + f)|}}. \quad (2)$$

In this study, the e-folding time of the initialized instability is approximately 5 h. Therefore, as no seeded perturbations are specified to trigger the release of the instability, and given that previous studies indicate that regions of inertial instability may be long-lived

(e.g. Sato & Dunkerton, 2002; Schultz & Knox, 2007; Thompson et al., 2018), simulations are run for 14 model days to allow sufficient time for the growth of meridional perturbations (i.e., the release of the instability).

3 Results

3.1 How the instability is released

The response of the atmosphere to the instability is illustrated with snapshots of the horizontal wind at 11 km for the 50 m s^{-1} jet simulation (Figure 2). The release of the instability does not become apparent until after 72 h, when the wind maximum increases by 5 m s^{-1} between 72 and 96 h (Figures 2a,b), then holds mostly steady afterward. During the same period, winds on the equatorward side of the jet accelerate and veer cyclonically, becoming almost perpendicular to the jet axis by 120 h near $y = 500$ km (Figures 2b,c).

A vertical cross-section taken at $x = 2000$ km shows the release of the instability in the meridional- and vertical-wind components within the equatorward side of the jet (Figures 2d–i). By 72 h, flat perturbations in the wind field develop in the center of the region of instability within the equatorward side with spatial scales of about 100 km in the meridional and 0.2 km in the vertical (Figures 2d,g). The vertical scale is comparable to the 0.2 km vertical grid spacing, a result also found by O'Sullivan and Hitchman (1992) and Blanchard et al. (1998). By 96 h, these perturbations have grown in the meridional direction to about 500 km and with perturbation horizontal meridional wind speeds of up to 7 m s^{-1} and vertical wind speeds of up to 2 cm s^{-1} (Figures 2e,h). These quasi-flat perturbations in the meridional wind develop as ribbons that alternate in direction with depth and span 8–13 km in the vertical by 120 h (Figure 2f). Thus, these circulations are hundreds of meters deep, hundreds of km in the north–south direction, and thousands of kilometers in the along-jet direction. Consequently, we call these ribbon-shaped circulations. The growing and expanding perturbations are quasi-stationary and largely confined to the initialized unstable region (Figure 1b). In contrast, perturbations in the vertical wind component expand rapidly outward from the initialized unstable region (Figures 2g–i), typically along isentropes.

After the release of the instability and the initial formation of the perturbations within the region of initial instability, inertia–gravity waves propagate laterally and ver-

tically away from the jet's equatorward side. Although inertia–gravity-wave emission is an expected consequence of unbalanced flow (e.g. Koch et al., 1988; Zhang et al., 2000; Plougonven & Zeitlin, 2009; Rowe & Hitchman, 2015), waves do not appear until 72 h and then appear concurrently with the meridional wind perturbations, indicating that they arise from the release of the instability.

In contrast to the 50 m s^{-1} simulation with an initialized region of instability, the 30 m s^{-1} simulation without any instability undergoes an entirely different evolution. The horizontal wind speed of the jet does not increase (not shown). Perturbations and inertia–gravity waves do not develop to any substantial degree. A direct comparison between the two simulations can be constructed by looking at a time–height cross section of averaged fields between $x = 1000$ km and $x = 2000$ km (Figure 3). Averaging along this 1000-km length illustrates that the perturbations develop along the length of the jet (i.e., the release of the instability is occurring on a large scale.) Over time, the meridional and vertical wind components show minimal perturbations growing for the 30 m s^{-1} simulation (Figures 3a,c). In contrast, the perturbations in the 50 m s^{-1} simulation grow within the region of the inertial instability initially after about 24 h, but most substantially after 72 h (Figures 3b,d). Within the center of the region of the initialized instability, the perturbations have vertical wavelengths of 0.5 km during 72–120 h, but after about 96 h, perturbations at heights of 9 and 13 km have developed with a larger vertical wavelength of 1.5 km (Figure 3b). These larger wavelength features persist for about 11 days until the end of the simulation as inertia–gravity waves also radiate away from the jet.

3.2 Relationship to observations and simulations

These model simulations suggest how an inertially unstable region near midlatitude jet streams evolves. In this section, we compare our results to observations and other simulations of the release of inertial instability.

First, we showed that the winds on the equatorward side of the jet turned increasingly equatorward to help weaken the anticyclonic shear. Such a result is common at the jet-exit regions of tropospheric jet streams, leading to anticyclonic Rossby-wave breaking in the troposphere (e.g. Postel & Hitchman, 1999), as well as in the stratosphere (e.g. O'Sullivan & Hitchman, 1992; Knox & Harvey, 2005). In this way, our results bear some

similarity to observations. However, our results were inconsistent with those of Rowe and Hitchman (2015, 2016) who found similar local wind maxima in simulations of extratropical cyclones. Whereas they found the inertially unstable flow accelerating poleward, we found it accelerating equatorward. It is unclear why there is an inconsistency.

Second, the release of the instability was indicated by the presence of layered circulations that remained within the region of the instability. Although such layers are a classic signature of inertial instability release in the stratosphere (Hitchman et al., 1987; Hayashi et al., 2002; O'Sullivan & Hitchman, 1992; Harvey & Knox, 2019), observational evidence of the release of inertial instability in the troposphere remains sparse. In the most compelling case, Sato and Dunkerton (2002) highlight stationary alternating layers in the meridional wind of up to 7 m s^{-1} over an 8-km layer that lasted for at least a week over southern Japan. This meridional wind speed is consistent with that of our study where meridional wind speeds of up to 7 m s^{-1} occurred in the model (Figures 2e,h). Noting that these layers often occur within regions of weak or negative potential vorticity on the anticyclonic side of the westerly jet stream, they suggest that the observed layers are likely due to the release of inertial instability. These circulations also expand horizontally, more so in the cross-jet direction than along the jet, and in the vertical, matching results from idealized modeling (Griffiths, 2003; Plougonven & Zeitlin, 2009). Given the similarities to perturbations described here, the release of inertial instability in the real atmosphere appears to be reproduced in the present simulations.

Third, the release of the inertial instability in the localized region of the instability was followed by the emission of inertia–gravity waves, as seen in idealized simulations (Kloosterziel et al., 2007; Plougonven & Zeitlin, 2009; Carnevale et al., 2013; Ribstein et al., 2014; Kloosterziel et al., 2015). The inertia–gravity waves produced weaker perturbations than the release of the inertial instability (Plougonven & Zeitlin, 2009). These results show that the release of inertial instability initially occurs in a localized region followed by the emission and nonlocal radiation of inertia–gravity waves; both of these phenomena can lead to clear-air turbulence. Furthermore, Rapp et al. (2018) and Harvey and Knox (2019) have cautioned about conflating inertial instability release and inertia–gravity waves (albeit in the temperature field) and advocate for a large-scale examination of the meteorological conditions to better distinguish the two. As perturbations arising from inertial instability remain quasi-stationary (Hitchman et al., 1987; Sato & Dunkerton, 2002; Knox, 2003), as also seen here, we identify both inertial-instability release and

inertia–gravity waves, and attribute the former as a source of inertia–gravity-wave emission.

3.3 Clear-air turbulence

One hypothesized impact from the release of inertial instability is that any associated inertial-gravity waves could lead to clear-air turbulence (CAT) when these waves break (Knox, 1997). Although we find no evidence of CAT due to inertia-gravity waves in these simulations, the layered circulations themselves resulting from inertial instability release produce CAT, as diagnosed by the Ellrod–Knapp Turbulence Index (Ellrod & Knapp, 1992). The Ellrod–Knapp Index (3) is a CAT diagnostic used by several aviation forecasting centers around the world that combines flow deformation, convergence, and vertical wind shear into a single parameter, capable of detecting 70–84% of CAT occurrences (Ellrod & Knapp, 1992; Sharman & Pearson, 2017; Kim et al., 2018; Gultepe et al., 2019). This index was calculated in the standard way, as

$$TI = VWS \times (DEF + CGV) \tag{3}$$

$$VWS = \frac{dV}{dx} \qquad DEF = \sqrt{DSH^2 + DST^2} \tag{4}$$

$$DSH = \frac{dv}{dx} + \frac{du}{dy} \qquad DST = \frac{dv}{dx} + \frac{du}{dy} \tag{5}$$

$$CVG = -\left(\frac{du}{dx} + \frac{dv}{dy}\right). \tag{6}$$

where TI stands for turbulence index, VWS is the vertical wind shear, DEF is the total deformation, DSH is the shearing deformation, DST is the stretching deformation, and CVG is the horizontal convergence. Calculating this index from CM1 zonal and meridional winds, we find CAT develops simultaneously with the meridional wind perturbations on the equatorward side of the 50 m s^{-1} jet over a three-day period between 84 h and 156 h. The turbulence does not develop as a single continuous area, but in sporadic pockets of light–moderate intensity that persist for up to 12 h around the periphery of the unstable region (Figure 4a). Collating all turbulence occurrences throughout the simulation, we find that most occurrences fall into this light–moderate category, but some occurrences of moderate intensity are also found (Figure 4b). Whether this result could

translate into an application in aviation forecasting, however, still depends on it being reproducible outside of an idealized modeling context.

4 Summary

The release of inertial instability, defined as negative absolute vorticity in the Northern Hemisphere, has been investigated for an idealized jet stream. Two simulations of a zonal midlatitude jet—one with inertial instability on the equatorward side and one with inertial stability on the equatorward side—have been performed to show how the instability is released.

We find that when an inertially unstable region is initialized in the model, jet-maximum winds increase by 5 m s^{-1} after a few days and westerly winds on the equatorward side of the jet accelerate and veer equatorward. Additionally, quasi-stationary zonally-elongated meridional wind perturbations grow to dimensions of about 500 km and 0.5 km in the zonal and vertical directions, respectively, with magnitudes of up to 7 m s^{-1} in the meridional and 2 cm s^{-1} in the vertical. These ribbon-like perturbations grow in coverage to occupy much of the region of inertial instability and persist for 11 days. Shortly after the formation of these ribbons of enhanced meridional wind, inertia–gravity waves radiate away from the inertially unstable region in an X-shaped region away from the jet. These results thus show how inertially unstable flow on the equatorward side of jet streams breaks down into inertia–gravity waves and ribbons of enhanced meridional wind that counteracts the strong anticyclonic shear that defined the instability. Furthermore, our simulations highlight the release of inertial instability as a source of light–moderate occurrences of CAT, meriting further investigation into its prevalence in the real atmosphere and its potential utility to aviation forecasting.

In this letter, we have established the following. First, we have shown that the observational findings of Sato and Dunkerton (2002) are consistent with the release of inertial instability in the troposphere. Second, inertial instability release in the troposphere is similar to that in the stratosphere in terms of meridional wind perturbations and the emission of gravity waves. Finally, we have shown that the release of inertial instability promotes light–moderate occurrences of clear-air turbulence.

Acknowledgments

We thank George Bryan of the National Center for Atmospheric Research for providing the source code for the zonal jet initialization. We thank the two anonymous reviewers for comments that improved this manuscript. Callum Thompson was funded in part by the National Environmental Research Council's Understanding the Earth, Atmosphere, and Ocean Doctoral Training Programme, Grant NE/L002469/1. Partial funding for Schultz was provided by the Natural Environment Research Council Grants NE/I026545/1 and NE/N003918/1 to the University of Manchester. Model output for the two simulations will be made available through the University of Manchester Research Data Archive Storage; in the meantime, all data and scripts can be obtained by sending an email to the lead author: thompson.callum@yahoo.co.uk.

References

Blanchard, D. O., Cotton, W. R., & Brown, J. M. (1998). Mesoscale circulation growth under conditions of weak inertial instability. *Mon. Wea. Rev.*, *126*, 118–140. doi: 10.1175/1520-0493(1998)126⟨0118:MCGUCO⟩2.0.CO;2

Blumen, W., & Washington, W. M. (1969). The effect of horizontal shear flow on geostrophic adjustment in a barotropic fluid. *Tellus*, *21*, 167–176. doi: 10.1111/j.2153-3490.1969.tb00428.x

Bryan, G. H., & Fritsch, J. M. (2002). A benchmark simulation for moist nonhydrostatic numerical models. *Mon. Wea. Rev.*, *130*(12), 2917–2928. doi: 10.1175/1520-0493(2002)130⟨2917:ABSFMN⟩2.0.CO;2

Carnevale, G. F., Kloosterziel, R. C., & Orlandi, P. (2013). Inertial and barotropic instabilities of a free current in three-dimensional rotating flow. *J. Fluid Mech.*, *725*, 117–151.

Coniglio, M. C., Hwang, J. Y., & Stensrud, D. J. (2010). Environmental factors in the upscale growth and longevity of MCSs derived from rapid update cycle analyses. *Mon. Wea. Rev.*, *138*, 3514–3539. doi: 10.1175/2010MWR3233.1

Ellrod, G. P., & Knapp, D. I. (1992). An Objective Clear-Air Turbulence Forecasting Technique: Verification and Operational Use. *Wea. Forecasting*, *7*, 150–165. doi: 10.1175/1520-0434(1992)007⟨0150:AOCATF⟩2.0.CO;2

Fultz, A. J., & Ashley, W. S. (2016). Fatal weather-related general aviation accidents in the united states. *Phys. Geogr.,*, *37*, 291–312. doi: doi:10.1080/

02723646.2016.1211854

Griffiths, S. D. (2003). Nonlinear vertical scale selection in equatorial inertial instability. *J. Atmos. Sci.*, *60*, 977–990. doi: 10.1175/1520-0469(2003)060⟨0977:NVSSIE⟩2.0.CO;2

Gultepe, I., Sharman, R., Williams, P. D., Zhou, B., Ellrod, G., Minnis, P., ... Neto, F. L. A. (2019). A review of high impact weather for aviation meteorology. *Pure Appl. Geophys.*, *176*, 1869–1921. doi: 10.1007/s00024-019-02168-6

Han, J., Witek, M. L., Teixeira, J., Sun, R., Pan, H.-L., Fletcher, J. K., & Bretherton, C. S. (2016). Implementation in the ncep gfs of a hybrid eddy-diffusivity mass-flux (edmf) boundary layer parameterization with dissipative heating and modified stable boundary layer mixing. *Wea. Forecasting*, *31*(1), 341–352. doi: 10.1175/WAF-D-15-0053.1

Harvey, V., & Knox, J. (2019). Beware of inertial instability masquerading as gravity waves in stratospheric temperature perturbations. *Geophys. Res. Lett.*, *46*, 1740–1745. doi: 10.1029/2018GL081142

Hayashi, H., Shiotani, M., & Gille, J. C. (2002). Horizontal wind disturbances induced by inertial instability in the equatorial middle atmosphere as seen in rocketsonde observations. *J. Geophys. Res.*, *107*, 4228–4228. doi: 10.1029/2001JD000922

Hitchman, M. H., Leovy, C. B., Gille, J. C., & Bailey, P. L. (1987). Quasi-stationary zonally asymmetric circulations in the equatorial lower mesosphere. *J. Atmos. Sci.*, *44*, 2219–2236. doi: 10.1175/1520-0469(1987)044⟨2219:QSZACI⟩2.0.CO;2

Holton, J. R. (2012). *An Introduction to Dynamic Meteorology, 5th ed.* Academic Press.

Kim, J.-H., Sharman, R., Strahan, M., Scheck, J. W., Bartholomew, C., Cheung, J. C. H., ... Gait, N. (2018). Improvements in nonconvective aviation turbulence prediction for the world area forecast system. *Bulletin of the American Meteorological Society*, *99*, 2295–2311. doi: 10.1175/BAMS-D-17-0117.1

Kloosterziel, R. C., Carnevale, G. F., & Orlandi, P. (2007). Inertial instability in rotating and stratified fluids: Barotropic vortices. *J. Fluid Mech.*, *583*, 379–412.

Kloosterziel, R. C., Orlandi, P., & Carnevale, G. F. (2015). Saturation of equatorial inertial instability. *J. Fluid Mech.*, *767*, 562–594.

Knox, J. A. (1997). Possible mechanisms of clear-air turbulence in strongly anticyclonic flows. *Mon. Wea. Rev.*, *125*, 1251–1259. doi: 10.1175/1520-0493(1997)125⟨1251:PMOCAT⟩2.0.CO;2

Knox, J. A. (2003). Inertial instability. In J. Holton J. Pyle & J. Curry (Eds.), *Encyclopedia of the Atmospheric Sciences* (pp. 1004–1013). Academic Press.

Knox, J. A., & Harvey, V. L. (2005). Global climatology of inertial instability and Rossby wave breaking in the stratosphere. *J. Geophys. Res.*, *110*, D06108. doi: 10.1029/2004JD005068

Koch, S. E., Golus, R. E., & Dorian, P. B. (1988). A mesoscale gravity wave event observed during CCOPE. Part II: Interactions between mesoscale convective systems and the antecedent waves. *Mon. Wea. Rev.*, *116*(12), 2545–2569. doi: 10.1175/1520-0493(1988)116⟨2545:AMGWEO⟩2.0.CO;2

Leary, C. (1974). Comment on "Anomalous gradient winds: Existence and implications". *Mon. Wea. Rev.*, *102*, 257–257. doi: 10.1175/1520-0493(1974)102⟨0257:COGWEA⟩2.0.CO;2

O'Sullivan, D. J., & Hitchman, M. H. (1992). Inertial instability and rossby wave breaking in a numerical model. *J. Atmos. Sci.*, *49*(12), 991–1002. doi: 10.1175/1520-0469(1992)049⟨0991:IIARWB⟩2.0.CO;2

Plougonven, R., & Snyder, C. (2005). Gravity waves excited by jets: Propagation versus generation. *Geophys. Res. Lett.*, *32*, L18802. doi: 10.1029/2005GL023730

Plougonven, R., & Zeitlin, V. (2009). Nonlinear development of inertial instability in a barotropic shear. *Phys. Fluids*, *21*, 106601-1–106601-15.

Postel, G. A., & Hitchman, M. H. (1999). A Climatology of Rossby Wave Breaking along the Subtropical Tropopause. *J. Atmos. Sci.*, *56*, 359–373. doi: 10.1175/1520-0469(1999)056⟨0359:ACORWB⟩2.0.CO;2

Rapp, M., Dörnbrack, A., & Preusse, P. (2018). Large midlatitude stratospheric temperature variability caused by inertial instability: A potential source of bias for gravity wave climatologies. *Geophys. Res. Lett.*, *45*, 10,682–10,690. doi: 10.1029/2018GL079142

Raymond, D. J., & Jiang, H. (1990). A theory for long-lived mesoscale convective systems. *J. Atmos. Sci.*, *47*, 3067–3077.

Ribstein, B., Plougonven, R., & Zeitlin, V. (2014). Inertial versus baroclinic insta-

bility of the Bickley jet in continuously stratified rotating fluid. *J. Fluid Mech.*, *743*, 1–31.

Rowe, S. M., & Hitchman, M. H. (2015). On the role of inertial instability in stratosphere–troposphere exchange near midlatitude cyclones. *J. Atmos. Sci.*, *72*, 2131–2151. doi: 10.1175/JAS-D-14-0210.1

Rowe, S. M., & Hitchman, M. H. (2016). On the relationship between inertial instability, poleward momentum surges, and jet intensifications near midlatitude cyclones. *J. Atmos. Sci.*, *73*, 2299–2315. doi: 10.1175/JAS-D-15-0183.1

Sato, K., & Dunkerton, T. J. (2002). Layered structure associated with low potential vorticity near the tropopause seen in high-resolution radiosondes over Japan. *J. Atmos. Sci.*, *59*, 2782–2800. doi: 10.1175/1520-0469(2002)059⟨2782:LSAWLP⟩2.0.CO;2

Schultz, D. M., & Knox, J. A. (2007). Banded convection caused by frontogenesis in a conditionally, symmetrically, and inertially unstable environment. *Mon. Wea. Rev.*, *135*, 2095–2110. doi: 10.1175/MWR3400.1

Schumacher, R. S., & Schultz, D. M. (2001). Inertial instability: Climatology and possible relationship to severe weather predictability. In *Preprints, ninth conference on mesoscale processes* (pp. 372–375). Fort Lauderdale, FL.

Schumacher, R. S., Schultz, D. M., & Knox, J. A. (2010). Convective snowbands downstream of the Rocky Mountains in an environment with conditional, dry symmetric, and inertial instabilities. *Mon. Wea. Rev.*, *138*, 4416–4438. doi: 10.1175/2010MWR3334.1

Schumacher, R. S., Schultz, D. M., & Knox, J. A. (2015). Influence of terrain resolution on banded convection in the lee of the rocky mountains. *Mon. Wea. Rev.*, *143*, 1399–1416. doi: 10.1175/MWR-D-14-00255.1

Sharman, R. D., & Pearson, J. (2017). Prediction of energy dissipation rates for aviation turbulence. part i: Forecasting nonconvective turbulence. *J. Appl. Meteor. Climatol.*, *56*, 317–337.

Sharman, R. D., Trier, S. B., Lane, T. P., & Doyle, J. D. (2012). Sources and dynamics of turbulence in the upper troposphere and lower stratosphere: A review. *Geophysical Research Letters*, *39*(12), L12803. doi: https://doi.org/10.1029/2012GL051996

Siedersleben, S. K., & Gohm, A. (2016). The missing link between terrain-induced

potential vorticity banners and banded convection. *Mon. Wea. Rev.*, *144*, 4063–4080. doi: 10.1175/MWR-D-16-0042.1

Terpstra, A., & Spengler, T. (2015). An initialization method for idealized channel simulations. *Mon. Wea. Rev.*, *143*, 2043–2051. doi: 10.1175/MWR-D-14-00248.1

Thompson, C. F., Schultz, D. M., & Vaughan, G. (2018). A global climatology of tropospheric inertial instability. *J. Atmos. Sci.*, *75*, 805–825. doi: 10.1175/JAS-D-17-0062.1

Zhang, F., Koch, S. E., Davis, C. A., & Kaplan, M. L. (2000). A survey of unbalanced flow diagnostics and their application. *Adv. Atmos. Sci.*, *17*, 1861-9533. doi: 10.1007/s00376-000-0001-1

Figure 1. Cross sections of the initialized zonal wind (coloured) and angular momentum (black contours) for the 30 m s^{-1} (a) and 50 m s^{-1} zonal jet simulations. Potential temperature (K) in (a) and (b) is represented by black contours and the hatched region in (b) indicates negative absolute vorticity (i.e., inertial instability).

Figure 2. Evolution of the 50 m s^{-1} zonal jet simulation at 72 h (left column), 96 h (middle column) and 120 h (right column) for the horizontal wind at 11 km (top row), meridional wind (middle row), and vertical wind (bottom row). The meridional and vertical wind is overlayed with the absolute vorticity (black contours). The meridional and vertical wind cross-sections are taken at $x = 2000$ km.

Figure 3. Height–time composites of meridional wind and vertical velocity for the 30 m s^{-1} jet simulation (left column) and the 50 m s^{-1} jet simulation (right column). Each field is averaged between 1000 and 2000 km in the longitudinal direction and over the z–y region that spans the initialized inertial instability from Figure 1.

Figure 4. Cross section of the Ellrod Turbulence Index for $x = 2000$ km at 99 h (a). Black contours denote the meridional wind from –4 to 4 m s^{-1} by 1 m s^{-1} with solid contours denoting positive values and dashed contours denoting negative values. For all model output times, turbulence indices throughout the entire simulation domain are collated into a histogram and colored by turbulence intensity according to Ellrod and Knapp (1992) (b).

Figure 4.

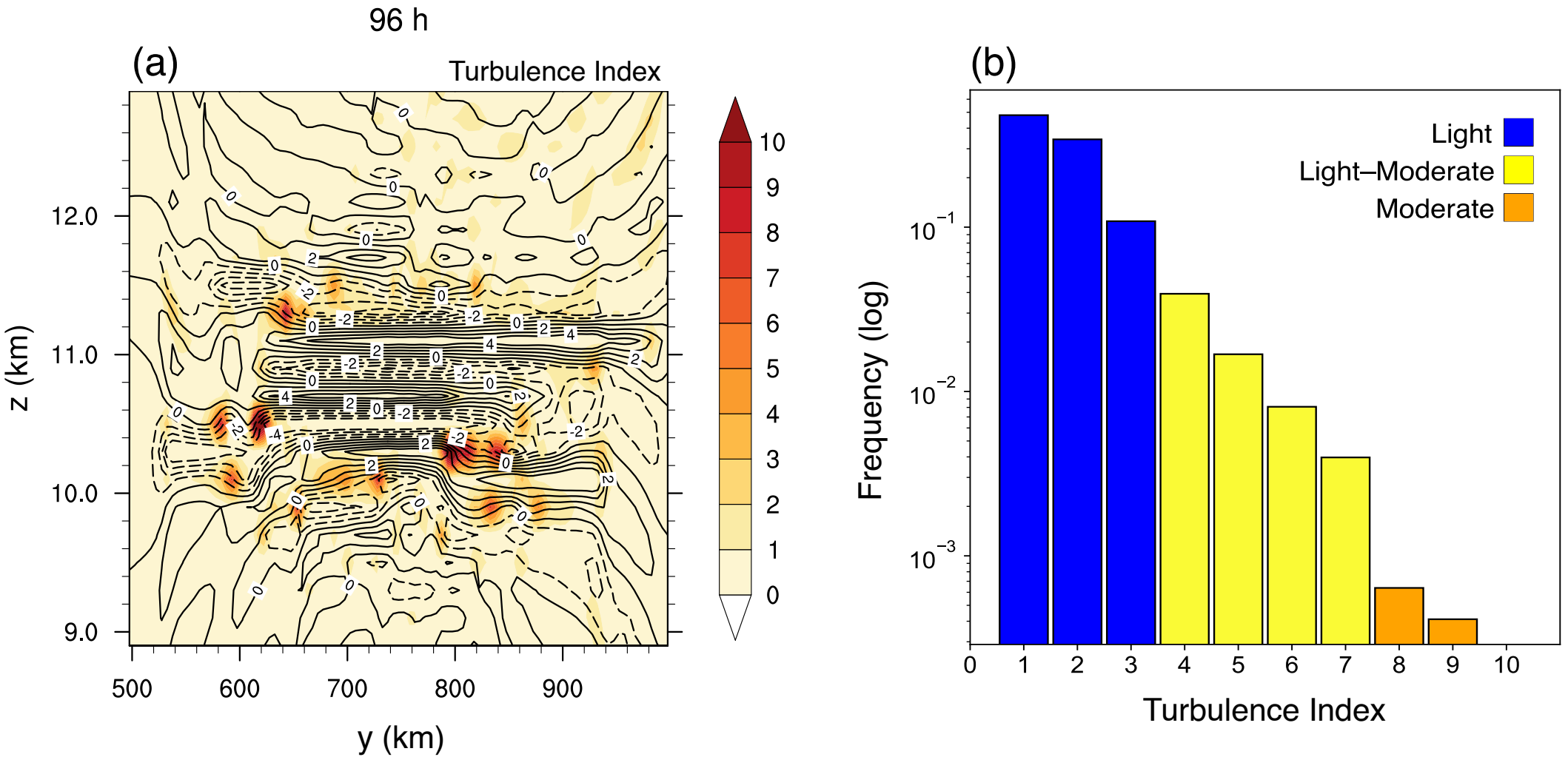
96 h
(a)
Turbulence Index
z (km)
y (km)
12.0
11.0
10.0
9.0
500
600
700
800
900
10
9
8
7
6
5
4
3
2
1
0
(b)
Frequency (log)
10^{-1}
10^{-2}
10^{-3}
Light
Light–Moderate
Moderate
0
1
2
3
4
5
6
7
8
9
10
Turbulence Index

Figure 3.

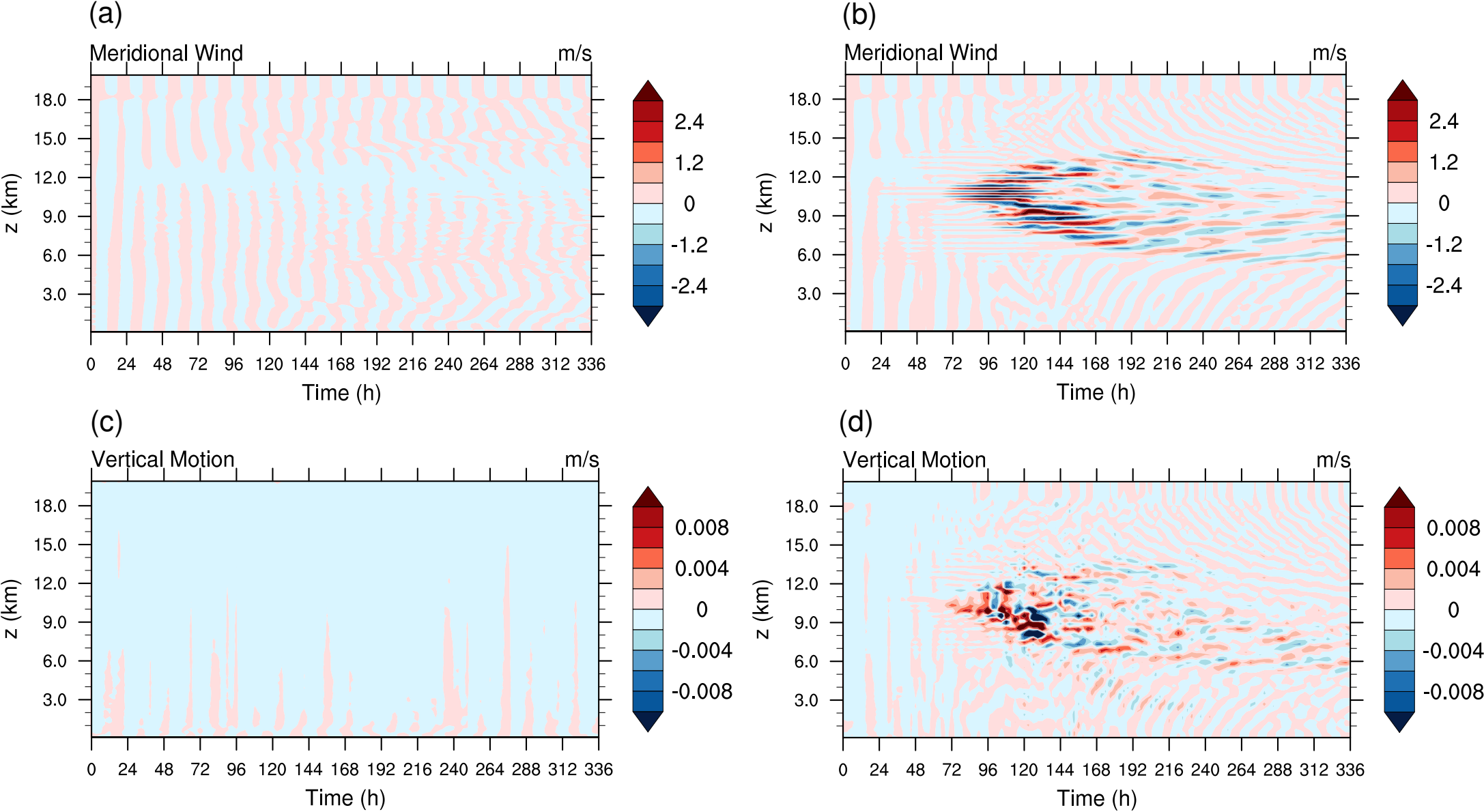
(a)
Meridional Wind
m/s
z (km)
18.0
15.0
12.0
9.0
6.0
3.0
0 24 48 72 96 120 144 168 192 216 240 264 288 312 336
Time (h)
2.4
1.2
0
-1.2
-2.4
(b)
Meridional Wind
m/s
z (km)
18.0
15.0
12.0
9.0
6.0
3.0
0 24 48 72 96 120 144 168 192 216 240 264 288 312 336
Time (h)
2.4
1.2
0
-1.2
-2.4
(c)
Vertical Motion
m/s
z (km)
18.0
15.0
12.0
9.0
6.0
3.0
0 24 48 72 96 120 144 168 192 216 240 264 288 312 336
Time (h)
0.008
0.004
0
-0.004
-0.008
(d)
Vertical Motion
m/s
z (km)
18.0
15.0
12.0
9.0
6.0
3.0
0 24 48 72 96 120 144 168 192 216 240 264 288 312 336
Time (h)
0.008
0.004
0
-0.004
-0.008

Figure 1.

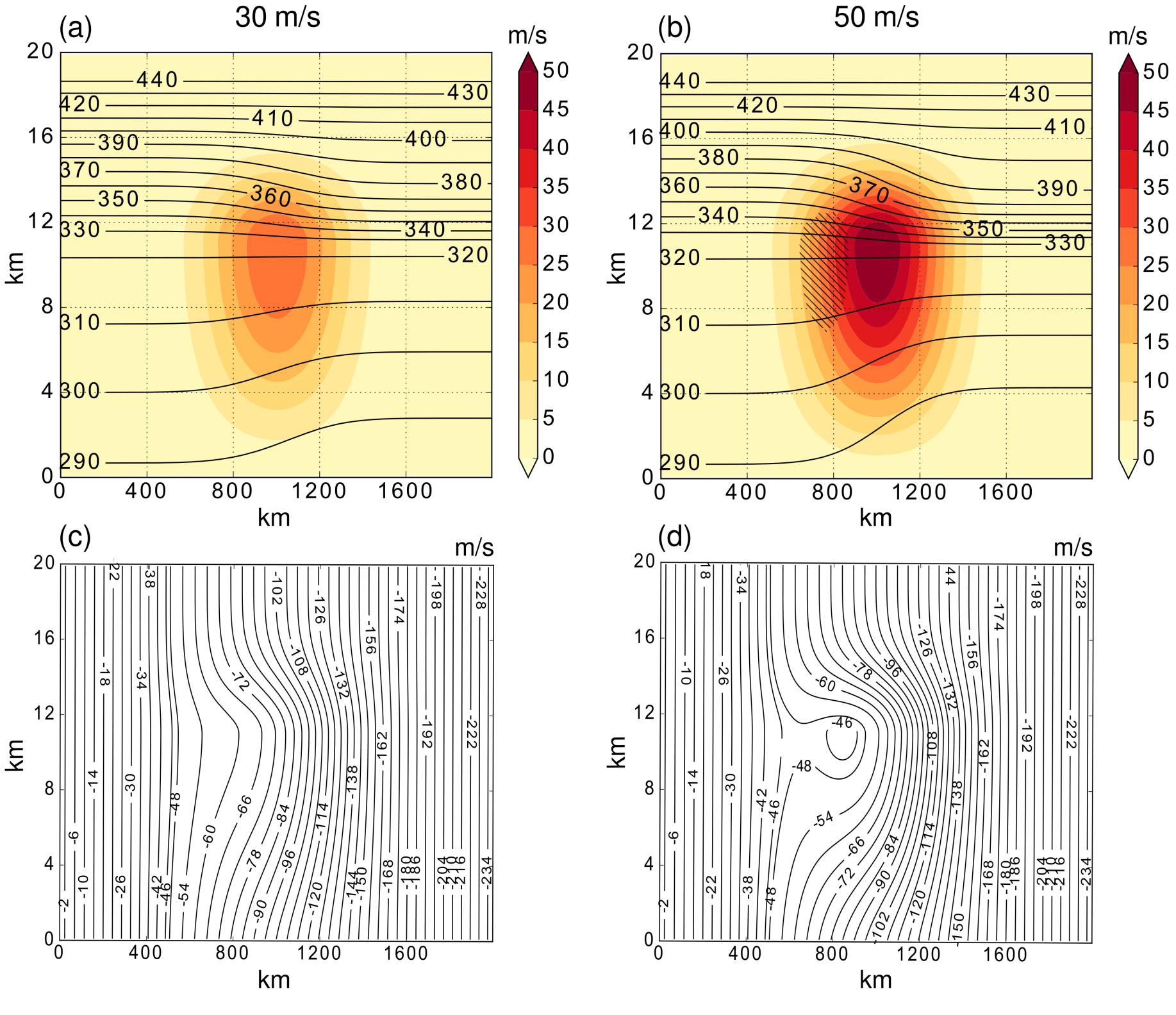
(a)
30 m/s
m/s
(b)
50 m/s
m/s
(c)
m/s
(d)
m/s
km
0
400
800
1200
1600
4
8
12
16
20
290
300
310
320
330
340
350
360
370
380
390
400
410
420
430
440
0
5
10
15
20
25
30
35
40
45
50

Figure 2.

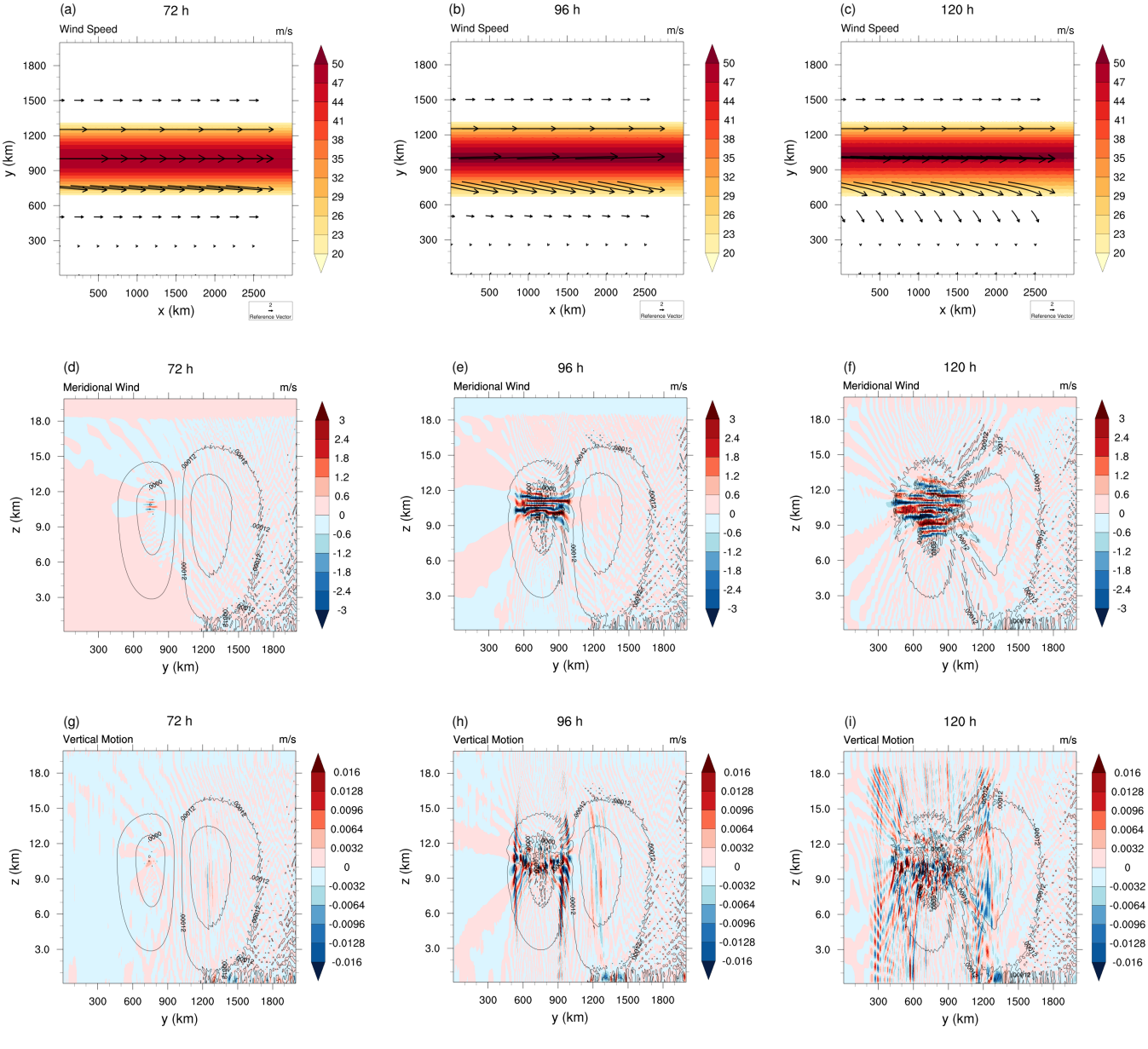
(a)
72 h
Wind Speed
m/s
y (km)
x (km)
Reference Vector
(b)
96 h
Wind Speed
m/s
y (km)
x (km)
Reference Vector
(c)
120 h
Wind Speed
m/s
y (km)
x (km)
Reference Vector
(d)
72 h
Meridional Wind
m/s
z (km)
y (km)
(e)
96 h
Meridional Wind
m/s
z (km)
y (km)
(f)
120 h
Meridional Wind
m/s
z (km)
y (km)
(g)
72 h
Vertical Motion
m/s
z (km)
y (km)
(h)
96 h
Vertical Motion
m/s
z (km)
y (km)
(i)
120 h
Vertical Motion
m/s
z (km)
y (km)